Mind of a dauer: Comparative connectomics reveals developmental plasticity

Hyunsoo Yim[1,6], Daniel T. Choe[1,6], J. Alexander Bae[2,6], Hae-Mook Kang[2], Ken C.Q. Nguyen[3], Myung-kyu Choi[1], Soungyub Ahn[1], Sang-kyu Bahn[4,7], Heeseung Yang[1], David H. Hall[3], Jinseop S. Kim[4,5,]*, Junho Lee[1,2,]*

1. Department of Biological Sciences, Seoul National University, Seoul, 08826, KR

2. Research Institute of Basic Sciences, Seoul National University, Seoul, 08826, KR

3. Department of Neuroscience, Albert Einstein College of Medicine, Bronx, NY, 10461, USA

4. Neural Circuits Research Group, Korea Brain Research Institute, Daegu, 41062, KR

5. Department of Biological Sciences, Sungkyunkwan University, Suwon-si, Gyeonggi-do, 16419, KR

6. These authors contributed equally to this work.

7. Present address: Cognitive Science Research Group, Korea Brain Research Institute, Daegu, 41062, KR

*Correspondence to: jinseopskim@skku.edu (J. S. K.), elegans@snu.ac.kr, (J. L.)

Abstract

A fundamental question in neurodevelopmental biology is how flexibly the nervous system can change during development. To address this question of developmental plasticity, we analyzed the connectome of dauer, an alternative developmental stage of nematodes with physiological and behavioral characteristics remarkably distinct from other developmental stages. We reconstructed the complete chemical connectome of a dauer by manual volumetric reconstruction and automated synapse detection using deep learning. While the basic architecture of the nervous system was preserved, there were also structural changes in neurons, large or small, that were closely associated with changes in the connectivity, some of which in turn evoked dauer-specific behaviors such as nictation. Combining the connectome data and optogenetic experiments were enough to reveal dauer-specific neural connections for the dauer-specific behavior. Graph theoretical analyses showed higher clustering of motor neurons and more feedback connections from motor to sensory neurons in the dauer connectome, suggesting that the dauer connectome allows a quick response to an ever-changing environment. We suggest that the nervous system in the nematode, which can be extended to animals in general, has evolved to obtain the ability to respond to harsh environments by reversibly developing a connectome quantitatively and qualitatively differentiated from other developmental stages.

When Sydney Brenner initiated his ambitious research on the connectome of the nematode *C. elegans* in the middle of the 20th century, one of his ultimate questions was how a nervous system governs behavior [1, 2]. Comparative connectomics provides excellent opportunities to answer this question. The origin of different behaviors at different life stages is being disclosed by the comparison of the developing connectomes. The nervous system of an alternative developmental stage called the dauer exhibits profound developmental plasticity. Under one or more unfavorable conditions including starvation, crowding, and heat stress, most nematode species at their early developmental stage commonly enter the diapause state and systematic anatomical changes occur to many tissues, acquiring physiological robustness and displaying various unique behavioral repertoires (Fig. 1a) [3-9]. The remodeling of the connectome underlying these behavioral changes will be of great interest in elucidating both the neural substrates of behaviors and the principles of animal development [10, 11].

In this study, we characterize the connectome of the hermaphrodite dauer nerve ring (Fig. 1a), where the arborization of neural processes and the synapses are most dense, in comparison with the connectomes of L1~L4 and adult stages in 10 datasets from previous studies shared in open source data (Extended Data Fig. 1a; [12-15]). The dauer connectome was obtained through an image acquisition and analysis pipeline, including serial-section transmission electron microscopy (ssTEM), volumetric reconstruction by manual segmentation, and complete annotation of chemical synapses using deep learning (Extended Data Figs. 1b, c).

Volumetric reconstruction of dauer brain

A *C. elegans* dauer nerve ring sample was sectioned and imaged at every 50 nm, resulting in 364 serial TEM images. The dense volumetric reconstruction (Fig. 1a, Extended Data Fig. 1b; Methods) yielded the processes of 181 neurons in the nerve ring, whose number is only modestly different from those of the other late developmental stages: 174 (L3), 180 (L4), 182 (adult), etc (Extended Data Fig. 1a). After the volumetric reconstruction and cell identification, we carefully observed the neural processes by visual inspection of the 3D rendering (Supplementary Table 1). We noticed the changes in dauer of varying magnitudes and forms, the most prominent of which were categorized into Branching (B), small Protrusion (P), Retraction (R), and Shrinkage (S) of the neurites and terminal swellings. Unlike the minor anatomical changes except for growth in size observed across other development stages [13], the changes in dauer were often more dramatic as shown in Extended Data Fig. 2

The IL2 neurons are a family of six sensory neurons, critical to the dauer-specific phoretic behavior called nictation; two of these are lateral cells and the rest are quadrant cells (dorsal and ventral)[1, 9]. Dauer IL2 lateral neurons add an extra branch that emerges perpendicularly from the apex of an axon

bend (Figs. 1b, c). Previous literature reported that while IL2 quadrant neurons undergo significant remodeling in their processes during dauer development, IL2 lateral neurons change less so [16]. Thanks to the finer resolution of TEM, we discovered that similar remodeling occurs in IL2 lateral neurons as well. As a cross-validation, we employed fluorescence microscopy to observe the IL2 lateral neurons in different stages including a post-dauer adult (Fig. 1c), confirming that the extra branches of IL2 lateral neurons appear only in dauer. In addition, the terminal swellings of IL2 lateral neurons were shrunken in dauer, losing contact with the IL2 dorsal neurons (Fig. 1b). The URB neurons (Fig. 1d) and RIH neurons (Fig. 1e) also show structural changes in dauer.

Completion of dauer chemical connectome

In order to correlate the morphological changes from volumetric reconstruction with changes in synaptic connections, we analyzed the full nerve ring connectome of the dauer. We annotated the chemical synapses in the image stack, yielding a complete connectivity map between the reconstructed neurons (Fig. 1a) [6, 13]. A convolutional neural network (CNN) was trained to label the active zones by referring to examples curated by human experts (Methods). The active zones were identified by the CNN and the labels over multiple serial sections were computationally merged into one 3D label for each chemical synapse. Each merged label was then proofread by human experts (Extended Data Figs. 1b, c; Methods). The postsynaptic partners of an active zone, together forming synapses, were assigned by simulating neurotransmitter diffusion to the closest neighboring axons as in previous studies (Methods; [13]).

All together, 2,813 active zones and 6,371 synapses were found in the dauer nerve ring (Extended Data Figs. 3a, b). Each active zone pairs with 2.26 postsynaptic partners on average (S. D.=0.93). 19% of the active zones form monadic and 81% polyadic synapses (Extended Data Fig. 3c). The 6,371 synapses form 2,200 connections, meaning that a pair of pre- and postsynaptic neurons are connected by 2.90 synapses on average (Extended Data Fig. 3d). As the size of the active zone could be a proxy for the functional strength of the synapse, the sum of active zone sizes is regarded as the connection weight or strength between two neurons. In summary, the dauer connectome is represented by a directed weighted graph with 181 nodes of neurons and 1,995 neuronal connections, or in total 2,200 connections including the neuromuscular junctions (Fig. 2a, Supplementary Table 2).

With the dauer connectome well established, we could now compare the connectivities of dauer with other stages from earlier studies (Extended Data Fig. 1a; [1, 12-15]). We found that the total number of connections in dauer nerve ring is similar to that of the adult nerve ring, thus deviating from the trend of linear gains with increasing larval ages (Fig. 2a; [13]). Comparisons across all developmental stages, including dauer, show 317 connections in common, which we call the “stage-conserved” connections (Fig. 2b). Another 499 connections exist only in the dauer, which we call the “dauer-

specific" connections (Fig. 2b; Supplementary Table 3). On the other hand, 31 connections exist only in other stages but not in dauer and we call these "dauer-loss" connections (Fig. 2b; Supplementary Table 3). Interestingly, dauer has over 25% of stage-specific connections, in contrast to the cases of other stages which have roughly 9% on average (Fig. 2c, Extended Data Fig. 3e). There are also many connections that are shared with other stages but with different connection weights in dauer (Fig. 2d). Wiring diagram differences of all individual neurons are in Supplementary Data 1.

Morphology to connectivity change

We examined whether the major morphological changes listed in Fig. 1 and Extended Data Fig. 2 were associated with the formation of new synapses (Extended Data Figs, 2, 3). We found that the IL2s with extra arbors as described above established new contacts and synapses of IL2→AUA and DVC→IL2 (Extended Data Fig. 4a, 4b). The dauer URB neuron received new synapses from IL1 on its new arbor on the dorsal side (Extended Data Fig. 4c), which forms one of the largest stage-specific connections in dauer (Extended Data Fig. 4d). RIH neurons grew 5 new branches, where a multitude of new synaptic inputs and outputs were made with various partners, among which the DVC→RIH synapse was notable (Extended Data Figs. 4e, f). Likewise, all the morphological changes described in Extended Data Fig. 2 were accompanied with the formation of new synaptic inputs and outputs.

Because small and ostensibly trivial morphological changes that are difficult to detect can also be associated with synaptic changes, we then inspected whether the connections with the largest changes are associated with any morphological changes underlying them. We found that, for most connection changes described in Fig. 2d, thickening of neural processes or broadening of local swellings contributed to the changes in contact and resulted in the establishment of new synapses. The connection with the largest weight among the dauer-specific connections and among all the dauer connections is ASG→ASI, both of which are amphid sensory neurons known to be involved in the dauer-entry decision [17]. The ASI→ASG connection weight was also highly increased in dauer (Supplementary Table 3). ASG and ASI do not form any synapse with each other in any reproductive stage although they do have several local contacts (Fig. 3a, top). At the same location in the dauer, a new swelling develops in ASI while ASG tightly adheres to the swelling, producing a larger contact and a new strong synapse (Fig. 3a, bottom). Including this location, the total ASI→ASG contact area in the dauer increased by a factor of 2.54 over the adult (Methods; Supplementary Table 4). An ASG connection to another neuron exhibits a large dauer weight loss. The ASG→AIA connection stands out among the 31 dauer-losses, as it is a high-weight connection in other developmental stages but totally disappeared in dauer (Fig. 3b). The size of the local swelling in AIA decreased and the contact area between AIA and ASG also decreased. Thus the total contact size between AIA and ASG was reduced by a factor of 0.33 in dauer compared to adult (Supplementary Table 4). The connection changes of ASG are summarized in Fig. 3c. We have observed similar correlation between

connectivity and contact in IL1 → RIC connection (Fig. 3d) and RIC → AVA and AVB connections (Fig. 3e). In dauer, the total contact between IL1 and RIC increased by a factor of 8.14, that of RIC→AVA decreased and RIC→AVB increased by a factor of 0.5 and 6.16, respectively. The changes involving RIC in the dauer are described in Fig. 3f.

Connection change drives dauer behavior

Next, we asked whether the connectional changes are associated with the unique behaviors of dauer. We considered the IL2 neurons first, which are known to play an essential role in nictation [9]. From the connectomes we found that IL2 quadrant neurons established strong connection to RIG neurons in the dauer (Fig. 4a). In dauer, each IL2 process forms a new swelling and a synapse with a large active zone forming at the new contact between the swellings of IL2 and RIG (Fig. 4b). Therefore, we hypothesized that RIG is a candidate neuron involved in the nictation behavior, acting downstream of IL2 neurons. To test this, we performed behavioral tests with dauers bearing mutations in two genes, *cha-1* and *daf-10*. Mutations in either gene results in the inactivation of IL2 neurons due to either acetylcholine synthesis defect or ciliogenesis defect[9]. The nictation ratio of *cha-1* and *daf-10* mutant dauers was significantly increased by optogenetic activation of RIG (Figs. 4c, d), suggesting that RIG activation was sufficient for the nictation of dauer even in the absence of ciliated, functional IL2 neurons, and that RIG neurons act downstream of IL2 in nictation. Therefore, an anatomical IL2→RIG connection in the dauer stage served as a functional connection. Another candidate neuron for dauer-specific physiology and behavior was the ASG neurons because the connections of ASG showed the most dramatic changes (Fig. 3a). We found that ASG-ablated worms exhibited poor nictation behavior compared to the control, suggesting that ASG is also required for nictation (Fig. 4e). In summary, our investigation of individual neuronal changes within the connectomes revealed that the changes in morphology and contact among neurons in dauer are closely associated with connectivity changes, which in turn evoke stage-specific behavioral changes.

Common network properties

Next, we compared the entire dauer connectome with connectomes of other stages statistically and systematically using graph theoretical analyses, seeking global characteristics of the dauer connectome. The connectomes of different stages have increasing numbers of connections with increasing ages and the dauer connectome has a similar number of connections as that of adults (Fig. 2a). Consistently, the average in- and out-degrees, directly indicating the number of connections per node, both show increase across developmental stages (Fig. 5a; [13]) along with other network measures. The dauer connectome appears to follow this tendency by showing similar values as in adults (Fig. 5). For simplicity, therefore, we will regard the dauer stage as part of later developmental stages in the following discussion on the tendency and correlation.

First, the clustering coefficient (CC), which measures the probability that the pair of neurons that are connected to a common neuron being connected to each other, displays a modest increase across development (Fig. 5b). The mean path length, the number of steps between a pair of neurons, decreases because connections added to a network provide shortcuts (Fig. 5c). Based on smaller mean path length and higher CC, we hypothesized that the later stage connectomes are small-world networks; thus, we quantitatively tested using two measures, small-worldness (ω) and small-world index (SWI; [18, 19]; Methods). While it is true that the neural network in all developmental stages have small-world properties [20], we can at most conclude that the correlation between the small-worldness of the whole network and developmental stages is uncertain due to discrepancy between two measures (P=0.001134 (ω), P=0.08764 (SWI); Fig. 5d). Still, it is worth noting smaller small-worldness in the later stages and dauer stage. This could be due to a more modularized structure of the network [13], meaning individual modules within a network could have small-world properties but this property is less obvious in the entire network.

The degree and weight distributions decay roughly exponentially, as revealed by the linear decrease in the semi-log plot (Fig. 5e). The exponential decay implies the network consists of a majority of peripheral neurons and only a few hub neurons such as RIH, AVB, AIB, and RIA. In addition, the distributions are shifted toward larger values and tails tend to become longer for dauer and later-stage networks (Fig. 5e), suggesting neurons with larger degree and weights like the hub neurons tend to have more connections in the dauer and later stages than they have in earlier stages. In summary, the dauer connectome shares common network properties with adult connectomes as revealed by the graph theoretical measures that capture the global network structures.

Enhanced motor to sensory feedback

Next, we further explored the details of common structures between dauer and later stages, which are distinguished from the early stages, by dissecting the networks into smaller parts. We first employed the 3 cell types, classified as sensory (S), inter- (I), or motor (M) neurons[12] to divide the connections into 3×3 = 9 different types according to the types of pre- and postsynaptic neurons. The proportions across all developmental stages showed a common pattern (Fig. 6a). The proportions of I to I connections (I→I) and S→I were highest and the proportions of M→I, M→S, and M→M connections were the lowest. It makes sense that the interneurons have large connectivity since they function as the center of communication, while the motor neurons have scarce outgoing connections to other neurons as they are supposedly the terminals of information flow. When we focus on the proportions of stage-specific connections, the baselines were elevated in the later-stage networks and the proportions of feedback connections were even higher within respective stages, among which the M→S proportion was most outstanding (Fig. 6b). In short, stage-specific connections of dauer and later stages contribute to enhancing feedback connections.

What would be the functional roles of the enhanced feedback connections? More feedback connections can shorten the path length (Fig. 5c) in the reverse direction of the canonical feedforward pathway, and short distances between neurons allow more intimate communication in networks. To investigate the roles of the later-stage feedback connections, we calculated the edge betweenness centrality (EBC), a measure for the importance of a connection in information flow (Methods). The EBCs were measured for all the connections in the networks of all stages and grouped according to the connection types. Also, the EBC distribution of dauer-specific connections was calculated by connection types. The feedback connections, especially M→S, exhibited the distributions with the largest EBCs when all connections were considered and even when only the dauer-specific connections were considered (Fig. 6c).

Since the main information flow of *C. elegans* occurs through the feedforward S→I→M paths and only a limited number of paths are connected backward (Fig. 6a), the feedback connections are apt to become the shortcuts of the network and become centralized in the perspective of betweenness as seen from above analysis. Beside from being the terminal neurons, the connections of motor neurons in dauer and later stages have an increased contribution in mediating signal processing compared to early stages.

Increased clustering of motor neurons

We then asked whether there are any unique characteristics of dauer. Referring to the proportions of stage-specific connections again, M→S, M→M, I→S, and S→I connections showed peaks in dauer (Fig. 6b). Among these, except for the previously discussed feedback connections, M→M connections were remarkable as it showed a peak only in dauer opposed to other later stages (Fig. 6b). Therefore, we next investigated how the dauer-specific M→M connections are organized.

To characterize the M→M connections, we considered three types of subnetworks, each consisting of one type of neurons and the connections between them. The motor subnetwork, composed of only the motor neurons and M→M connections, was analyzed in comparison to sensory and interneuron subnetworks. We first performed three-node motif analysis in each subnetwork and discovered that the proportions of the triangular motifs, where all the three neurons in a motif are connected to one another (Fig. 6d), were higher compared to the rest of the motifs. Therefore, we measured the summation of the proportions of the triangular motifs for all developmental stages in each subnetwork (Fig. 6d). As a reference, the triangular-motif proportions were also measured in the equivalent Erdős–Rényi (ER) random networks with the same number of nodes and average degrees. While the triangular-motif proportions had a roughly increasing trend across development in all three subnetworks, dauer deviated from this tendency by different degrees for each subnetwork (Fig. 6d). The proportion in dauer was the largest in motor subnetwork, indicating the connections of motor

neurons of dauer were found to make more triangular motifs compared to motor neurons of other stages and compared to sensory or interneurons of dauer. Moreover, this was also the case compared to what was expected from equivalent ER random networks and the difference in proportion between the real network and random networks was the largest in the dauer motor subnetwork. This is not fully explained by the connection proportion alone, as the connection proportions are similar in all developmental stages for intra-type connections (Fig. 6a). The evidence highlights that dauer motor neurons are specifically connected to make an exceptionally large number of triangles within each other.

As a validation, the CCs of the three subnetworks and the entire networks also showed increasing tendencies across development and notably the CC of the dauer motor subnetwork exhibited the distribution with largest values (Fig. 6e). This further supports the conclusion that dauer motor neurons are specifically connected for local clustering. The subnetwork diagrams of a few major motor neurons for adult and dauer exemplify that the dauer-specific connections enhance the proportion of triangular motifs and the clustering among motor neurons in dauer (Fig. 6f). In conclusion for the graph theoretical analyses, we conclude that there are enhanced feedback connections in later stages, including dauer, and increased clustering among motor neurons in dauer.

Discussion

C. elegans is a unique model organism for studying the nervous system because all animals contain the same set of neurons with an invariable number of exactly identifiable neurons, 302 in the case of hermaphrodite adults. In this study, we have shown that *C. elegans*, an animal with strictly fixed fate of cells, undergoes extensive remodeling of the nervous system during development in the alternative developmental stage, dauer. Complete stage-wise comparison of neural circuits at the single synapse level is now feasible with publicly available EM connectome datasets for all developmental stages ([1, 12-15]).

Resource for comparative connectomics

Morphological changes associated with synaptic changes must not be a mere coincidence but must be an event with concrete physiological advantages, because morphological remodeling is a highly energy-consuming process [21, 22]. The local morphological changes are permissive for connectional changes, and these changes can lead to valuable behavioral changes, even without changes in the number of neurons involved. The changes in morphologies and connections can be identified by comparative connectomics. The original question that Brenner posed, how the nervous system governs the behavior, can now be recast as the relationship between dauer-specific connections and unique behaviors of the dauer, which can be further explored by future experimental studies. One example is CO_2 sensing in different developmental stages. Consistent with a previous

report that AIY is not required for CO_2 response in dauers unlike adults [23], we easily identified that the connection from BAG [24], which is responsible for CO_2 detection to AIY does not exist in the dauer connectome while it exists in the adult (Supplementary Data 1). Now, it is possible to focus on additional specific connections and check how the neuronal functions differ in terms of CO_2 sensing using optogenetics and calcium imaging like the IL2-RIG experiments we have conducted. As these examples demonstrate, we believe that our new dauer connectome could lead to new discoveries of neural mechanisms for dauer-specific functions. Another example is the connection shift from RIC->AVA in other larval stages to RIC->AVB in the dauer. Proper analyses and experiments will reveal the significance of this shift in dauer-specific motility.

Few synapses are enough for new feedback

It has been reported that feedforward signaling increases in the later stages compared to the early stages by inspecting the proportion of synapses [13]. While our data showed that the proportion of connections do not differ significantly across development, including dauer (Fig. 6a), the proportions of feedback connections in later stages were higher than other connection types. Together, these results suggest that few synapses can be sufficient to create new stage-specific feedback connections while the increased number of synapses are more likely to strengthen existing feedforward connections in the later stages, especially in the dauer stage. Further studies are required on the functional strength or relevance of the connections with few synapses.

Wiring specificity as survival strategy

The qualitatively different network structures may support the survival strategies of the dauer. The enhanced clustering and augmented triangular motifs (Figs. 6e, f) can allow faster signal transduction by making shortcuts, can enhance the robustness in the signal processing by providing an alternative path, or can amplify the signal by making a cyclic, recurrent connection [25]. The abundant feedback connections toward sensory neurons (Figs. 6c, d), may also have functional importance in shaping the characteristic behaviors in later stages. Previous studies demonstrated that the feedback connections in the visual cortex aid distinction between low salience stimuli and background [26, 27]. Likewise, the feedback connections of the nematode may also enable filtering of the noise-rich signals amplified by the recurrent connections. The specificity in the connections of motor neurons may directly reveal the specificity in the behaviors. For instance, the neural circuit basis of the forward and backward locomotions has been uncovered as the reciprocal excitatory and inhibitory connections enabling the alternating activation and inactivation of the ventral and dorsal nerve cord motor neurons [28]. Similarly, the neural connections for the head exploration behavior could be found from the comparison of the motor neuron connectivity between dauer and other stages, since the dauer hardly performs the exploratory behavior [29]. Since the motor neurons analyzed in

this study are head motor neurons, the results discussed in this study would affect primarily head and neck movements. However, evidence suggests the links between head and body movements [30, 31], and the changes in the functionality of head motor neurons therefore could affect the body motions as well. As the nictation seems to be initiated in the nose and then propagate along the body, our nerve ring connectome may be useful in elucidating the mechanism of nictation.

In summary, as the last piece of the nematode connectome, we have reconstructed the first dauer nerve ring connectome from EM images, consisting of dense volumetric reconstructions of both neuronal and muscle cells, and their connectivity acquired using deep learning. Our dauer connectome resource will open up many possibilities to study how the neurons function differently due to differences in the neural circuit, and vice versa.

Figures

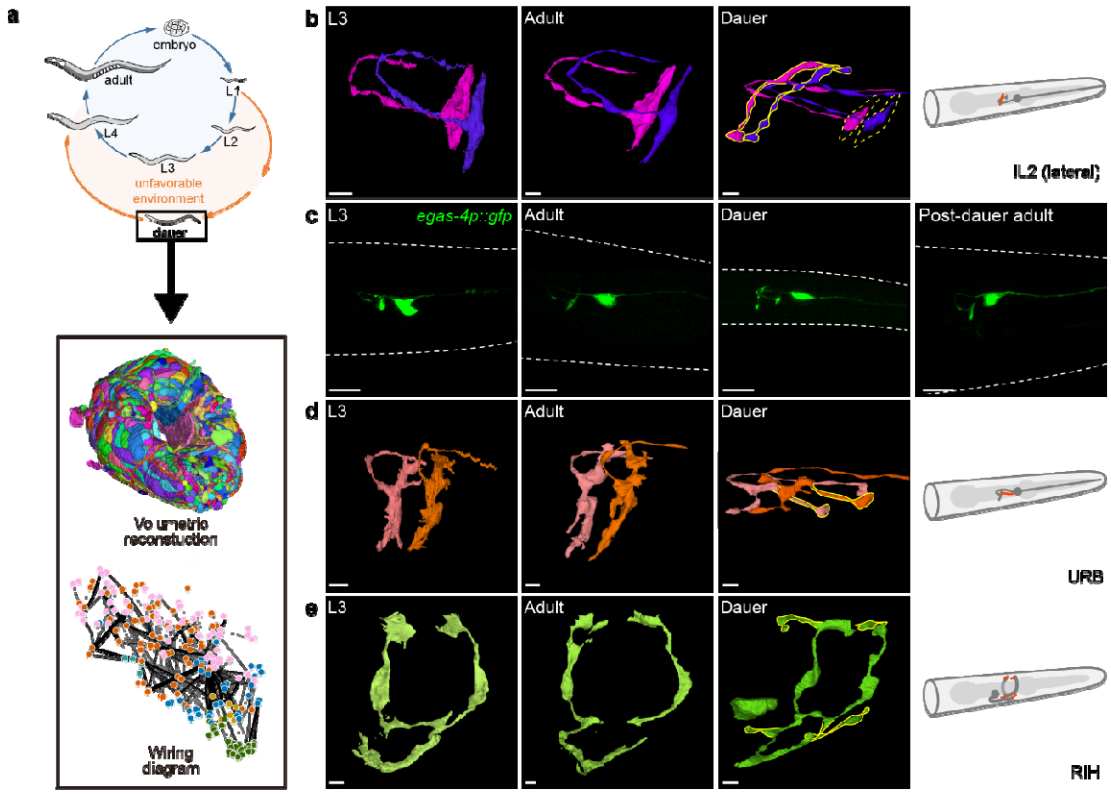

Fig. 1 Volumetric reconstruction of the dauer nerve ring.

a, A schematic that shows volumetric reconstruction and wiring diagram of dauer nerve ring.
b, Volumetric reconstruction of IL2 lateral neurons in L3, adult, dauer (from left) and schematic view of neuron in dauer stage (right). New branches emerge from the axon bend (solid yellow), and the terminal swelling shrinks (dashed yellow).
c, Fluorescence images of IL2 lateral neurons in L3, adult, dauer, and post-dauer adult (from left). Using *egas-4* promoter, IL2 lateral neurons were marked with GFP.
d, Same as (**b**) for URB neurons. New branches emerge from terminal swelling (solid yellow).
e, Same as (**b**) for RIH neurons. Small branches emerge from various regions (solid yellow).
(**b, d, and e**) Scale bar: 1 μm, (**c**) Scale bar: 10 μm.

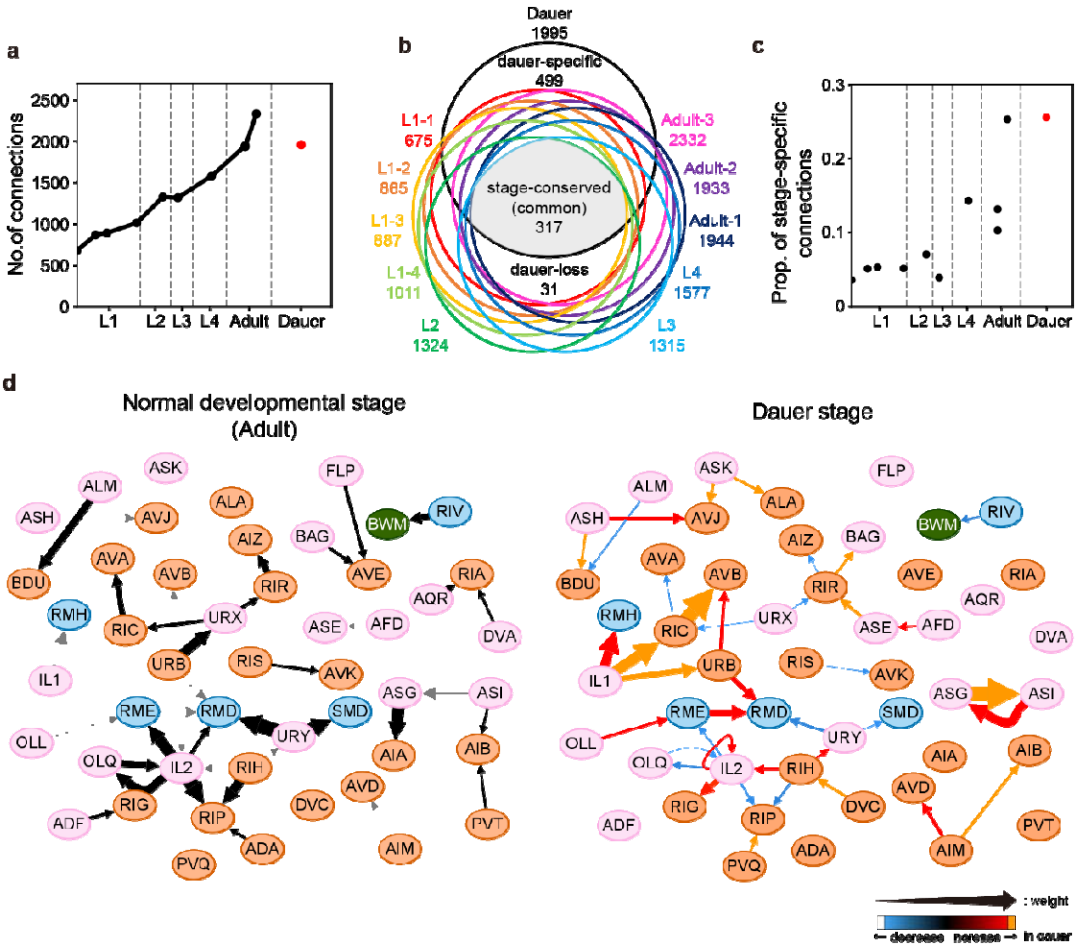

Fig. 2 Completion of dauer connectome.

a, Total number of connections between neurons in different developmental stages. Total number of connections in dauer is similar to that of an adult. **b,** Venn diagram of connections between neurons. 499 connections are connections that only exist in dauer. Area of each region is not scaled according to the number of connections for visual purposes. **c,** Proportion of stage-specific connections within each dataset. Over a quarter of connections are dauer-specific connections in dauer, which are considerably higher than other stages. **d,** Wiring diagram of representative changes in dauer connections (right) and wiring diagram of adult stage for the same set of neurons (left). The width of each arrow indicates the relative connection weight, normalized sum of all synapse weights involved in the connection (see Methods). Dauer-specific connections are represented with orange color arrows. Connections which the connection weights increased and decreased in dauer are represented with red and blue arrows, respectively. Color of the nodes represents cell types (pink: sensory neuron, orange: interneuron, blue: motor neuron, green: body wall muscle)

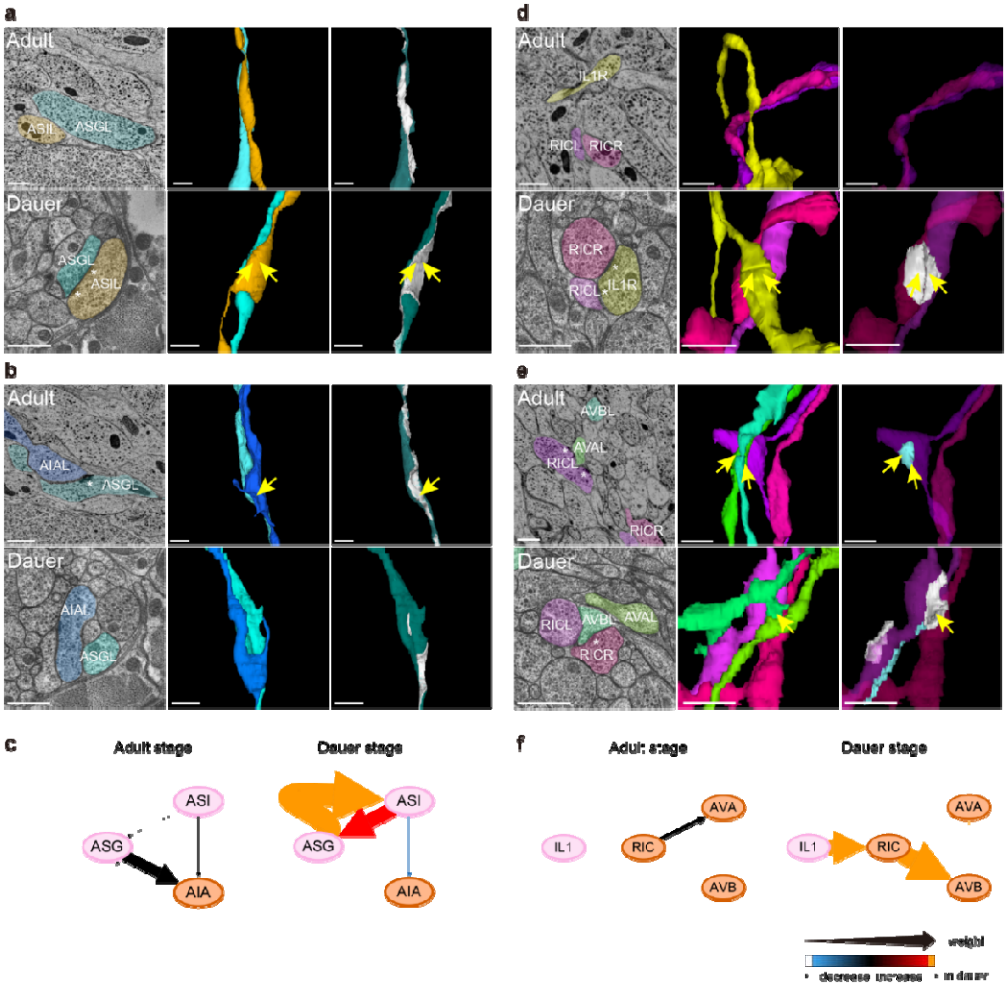

Fig. 3 Morphological changes and connectional changes are mutually associated.

a, EM cross-section view (left) and 3D volumetric reconstructions of presynaptic and postsynaptic neurons (middle) at the location of ASG-ASI contact where synapse exists. (right, contact area marked as white) in adult (top row) and dauer (bottom row). Contact area between ASG and ASI was significantly larger in dauer resulting in dauer-specific synapses (yellow arrows). Note that EM cross-section views of two stages may look different as two datasets have been sectioned in different orientations. **b,** Same with (**a**) for ASG-AIA contact. ASG-AIA contact area is significantly reduced in dauer while ASG-AIA contact area is distinctive resulting in larger synapse (yellow arrow). **c,** Wiring diagram of neurons shown in (**a**) and (**b**) in adult stage (left) and dauer stage (right). Width and color of the arrow follows the same rule from Figure 2D. Larger contact between ASG and ASI results in strong reciprocal connections and smaller contact between ASG and AIA results in no connection in dauer. **d,** Same with (**a**) for RIC-IL1 contact. IL1-RIC contact exists in the dauer stage while they do not make contact in the adult stage resulting in dauer-specific synapses (yellow arrows). **e,** Same with (**a**) for RIC-AVA (skyblue) and RIC-AVB (white) contacts. Area of RIC-AVA contact decreased in the dauer stage, leading to lack of synapses in the dauer stage while RIC-AVA synapses (yellow arrows) exist in the adult stage. Area of RIC-AVB contact increased in the dauer stage resulting in dauer-specific synapses (yellow arrow). **f,** Wiring diagram of neurons shown in (**d**) and (**e**) in adult stage (left) and dauer stage (right). Contact between RIC-IL1 and RIC-AVB results in new connections and lack of contact between RIC-AVA results in no connection in dauer.
(**a, b, d, e**) Scale bars: 500 nm (EM images), 1 µm (3D views). Asterisk: active zone.

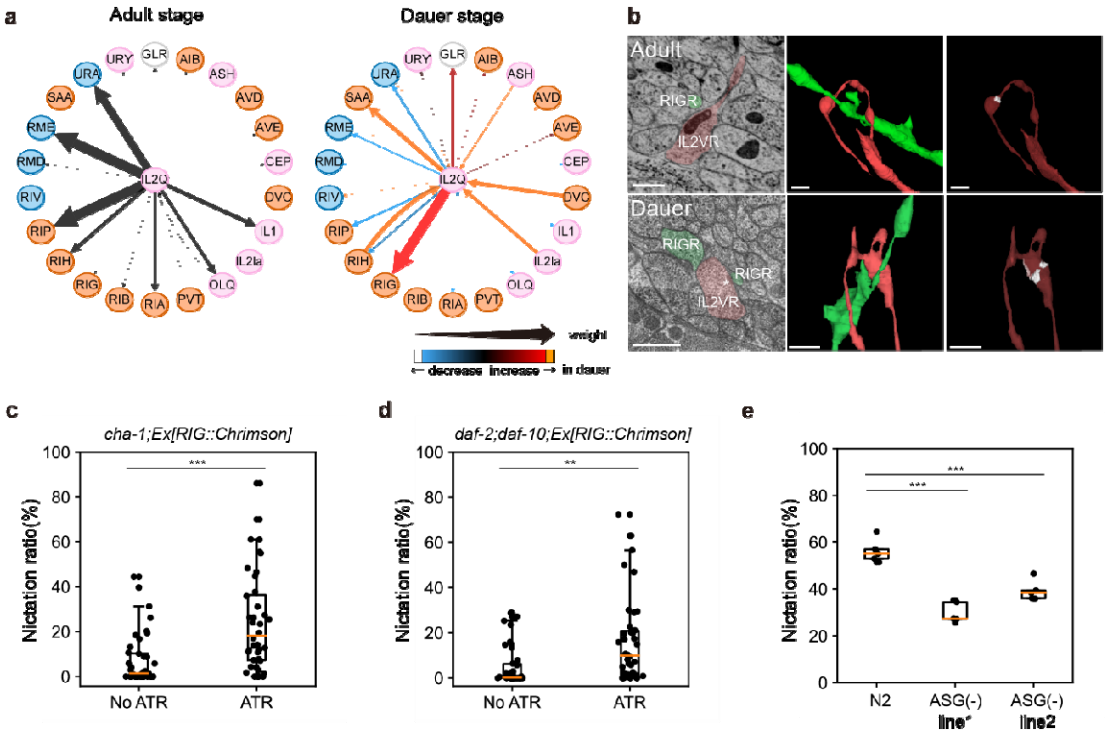

Fig. 4 Connectivity changes in dauer neurons are correlated with unique behaviors in dauer.

a, Wiring diagrams showing connections of IL2 quadrant neurons. Connection from IL2 to RIG showed significant increase in strength in the dauer stage. Width and color of the arrow follows the same rule from Figure 2D.
b, EM cross-section view (left) and 3D volumetric reconstructions of presynaptic and postsynaptic neurons (middle) at the location of IL2Q-RIG contact (right, contact area marked as white) in adult (top row) and dauer (bottom row).
c, RIG-activated cha-1 mutants exhibit significantly higher nictation ratio than cha-1 mutants (Individual nictation test; N=40, P<0.0001, unpaired t-test).
d, RIG-activated daf-2;daf-10 mutants exhibit significantly higher nictation ratio than daf-2;daf-10 mutants (Individual nictation test; N=38, P=0.0016, unpaired t-test).
e, ASG ablated lines show significantly lower nictation ratio than N2 (Population nictation test; 5 trials, n>60 worms in each experiment, P<0.0001, unpaired t-test).
(**b**) Scale bars: 500 nm (EM images), 1 μm (3D views). Asterisk: active zone. (**c, d, and e**) Red line: median, box: interquartile range, whisker: 5th and 95th percentiles.

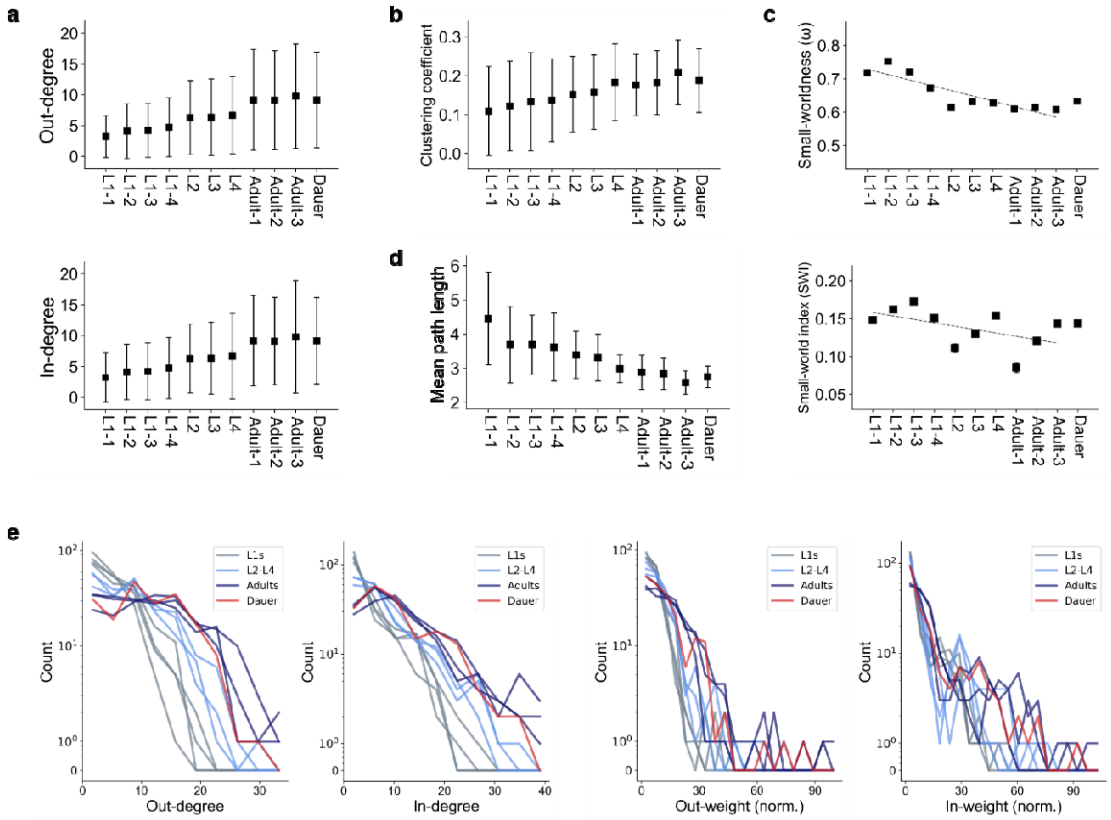

Fig. 5 The networks of dauer and later stages share common structural properties.

a, Out-degree (top) and in-degree (bottom) of neurons (mean±standard deviation (SD), *N*=187) across development. Both out-degree and in-degree show increasing trend as the worm matures and the dauer stage also show high out-degree and in-degree.
b, Clustering coefficient of neurons (mean±SD, *N*=187) across development. Clustering coefficient is measured based on connectivity between neurons. Clustering coefficient shows similar trend with out- and in-degree across development as shown in (a).
c, Distributions of mean path lengths of neurons (mean±SD, *N*=185) across development. Mean path length decreases as the worm matures and the dauer stage shows lower mean path length due to increased out- and in-degree.
d, Small-worldness (ω, top) and small-world index (SWI, bottom) across development. 100 random networks were generated to compute SWI (mean±SD, *N*=100, error bars may be hidden behind the square). Both small-worldness measurements show no significant trend across development (dotted line; P=0.001134 (ω), P=0.08764 (SWI), Pearson product-moment correlation coefficients). Datapoint for dauer was not included when measuring correlation due to ambiguity in proper position in development.
e, Histogram of out-degree, in-degree, normalized out-weights, and normalized in-weights (from left) of neurons. Degrees and weights for end organs are also included. Line color indicates developmental stages, grouped into four groups (gray: L1s, light blue: L2 to L4, dark blue: adults, red: dauer).

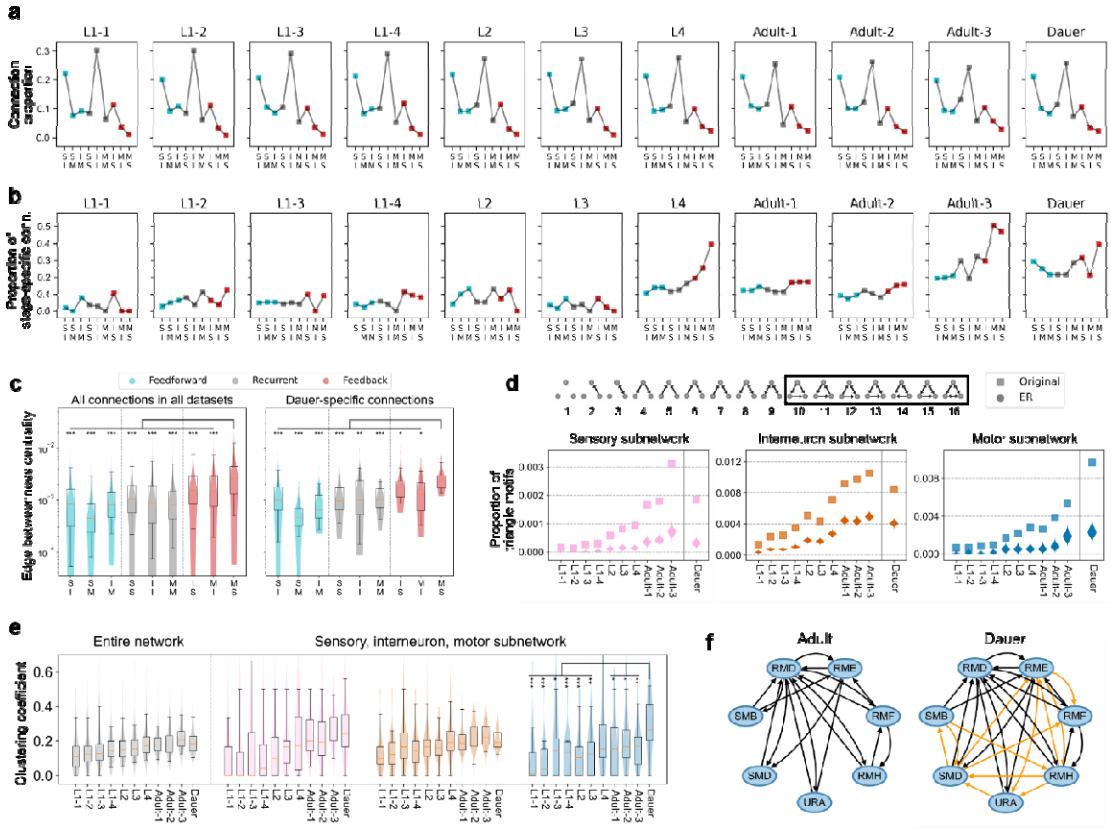

Fig. 6 Dauer connectome exhibits increased feedback and increased clustering within motor neurons.

a, Connection proportion of all connections. Connections between sensory (S) , inter- (I), and motor (M) neurons were assigned whether they are feedforward (cyan), recurrent (gray), or feedback (red) connections. Connection proportion distribution of different connection types are similar across development.
b, Proportion of stage-specific connections in each connection type. Feedback (red) connections have higher proportions of stage-specific connections in dauer and adult stages compared to feedforward (cyan) and recurrent (gray) connections.
c, Edge betweenness centrality distributions in different connection types for all connections from all stages (light) and dauer-specific connections (dark). M→S feedback connections have significantly higher edge betweenness centrality. Other feedback connections for all connections from all stages (M→I and I→S) also have significantly higher edge betweenness centrality. For dauer-specific connections however, M→I connections do not show significance for feedforward and recurrent connections (**P*<0.05, ***P*<0.01, ****P*<0.001, Wilcoxon rank-sum test).
d, Proportion of triangular motifs (motifs 10-16) by neuron types (square, pink: sensory, orange: inter, blue: motor) across development and that of Erdős–Rényi random networks (violin plot).
e, Distributions of clustering coefficient of neurons for the entire network (gray), sensory (pink), interneuron (orange), and motor (blue) subnetworks across development. Dauer exhibits significantly higher clustering coefficients in motor subnetwork (**P*<0.05, ***P*<0.01, ****P*<0.001, Wilcoxon rank-sum test).
f, Wiring diagram of representative motor neurons in the adult and dauer stages. Dauer motor neurons are more clustered due to dauer-specific connections (yellow). Connection weights are neglected for visual purposes.
(**c, d, e**) Red line: median, box: interquartile range, whiskers: 5th and 95th percentiles.

Extended Figure legends

Extended Data Fig. 1. Reconstruction pipeline and comparison with other datasets.

a, EM connectome datasets in different developmental stages used for comparison. The number of neurons present in the nerve ring increases as the worm matures. PVNR neuron already exists in the dauer stage while it does not exist until L4 stage and appears in the adult stage.
b, Reconstruction pipeline of dauer connectome. Electron microscopy (EM) image tiles were stitched and the stitched sections were aligned. From the aligned image stack, annotators manually traced and colored the area inside the membrane for each cell. Classes of reconstructed cells were identified according to morphological features. Chemical synapses were identified by detecting active zones in the EM images using convolutional neural network (CNN). For each active zone, the synaptic partners were assigned, giving a complete connectivity graph of reconstructed neurons.
c, Synapse detection in sample EM image cutout. Probability of pixels being in the darkly stained presynaptic active zones (yellow arrow) in the EM image (left) are predicted using CNN (middle, white indicates higher probability). Then for each predicted active zone, the probability values were thresholded and grouped using connected components to segment individual active zones (right, labeled with different colors). Lastly, manual proofreading has been done to remove falsely predicted active zones (red arrow) or falsely assigned active zones.

Extended Data Fig. 2. Morphological changes of neurons in the dauer stage.

Summary of representative morphological changes of neurons in the dauer stage with schematic. Morphological changes are classified into 4 types: branching (B), small protrusion (P), retraction (R), and shrinkage (S).

Extended Data Fig. 3. Connection properties across development.

a, Total number of active zones across development. L4 and adult-3 datasets are excluded as they do not provide synapse information.
b, Total number of synapses across development.
c, Average number of postsynaptic partners per active zone is consistent across development including the dauer stage (2.26 synapses per partner).
d, Total number of connections including neuromuscular junctions across development.
e, Normalized connection weight distribution of stage-specific connections in dauer dataset is larger than the distribution of stage-specific connections in adult-3 dataset (red line: median, box: interquartile range, whiskers: 5th and 95th percentiles; N=499, 589; P=0.0067, unpaired t-test) despite the similar level of stage-specific connection proportion.

Extended Data Fig. 4. Morphological changes are accompanied by new synaptic inputs and outputs.

a, 3D view of IL2 lateral neurons in dauer with new synaptic outputs and inputs (yellow arrow) in the region where morphological change occurred (solid yellow line).
b, Wiring diagram of IL2 lateral neurons in adult stage (top) and dauer stage (bottom). Width and color of the arrow follows the same rule from Figure 2D.
c, Same with (**a**) for URB neurons.
d, Same with (**b**) for URB neurons.
e, Same with (**a**) for RIH neurons.
f, Same with (**b**) for RIH neurons.
g, Normalized connection weight and contact sizes for 10 pairs of neurons with largest increase in connection weights (left) and largest decrease in connection weights (right) in dauer relative to adult-2 dataset.
(**a, c, and e**) Scale bar: 1 μm.

Supplementary Table 1. Neuroglancer link and segmentation key

Supplementary Table 2. Dauer connectivity matrix

Supplementary Table 3. Dauer-specific / dauer-loss / common connection lists.

Supplementary Table 4. Dauer contact matrix

Supplementary Data 1. Dauer wiring diagrams

Method

Experimental model and subject details

C. elegans were cultured and handled at 20°C according to standard methods [32] *C. elegans* strains used in this study are as follows: N2 Bristol. JN2113: Is2113[gcy-21p::mCaspase1, tax4p::nls::YC2.60, lin44p::GFP]. These strains were obtained from the Caenorhabditis Genetics Center (CGC). JN2114 (Is[gcy-21p::mCaspase, gcy-21p::mCherry, lin44p::GFP]) was provided by Iino Yuichi's lab. For TEM fixation, *C. elegans* Bristol strain N2 were used.

Dauer induction

For TEM fixation, seven to eight young adult larvae were transferred to synthetic pheromone plates containing agar (10□g/L), agarose (7□g/L), NaCl (2□g/L), KH2PO4 (3□g/L), K2HPO4 (0.5□g/L), cholesterol (8□mg/L), and synthetic pheromone-ascaroside 1, 2, 3 (2□mg/L each) [33, 34] seeded with Escherichia coli OP50 at 25□°C for dauer induction [35]. After 4 days, dauers were induced and morphologically identified by their radially constricted bodies and sizes. For nictation assay, only synthetic pheromone-ascaroside 2 (3□mg/L each) were used for dauer induction.

Fixation and staining for dauer larvae

Given the thicker cuticle on the dauer, we utilized an enhanced "OTO" protocol [36] to conduct multiple rounds of osmium tetroxide exposure following a high pressure freeze fixation to add extra layers of osmium stain prior to finishing a more regular counterstain with uranyl acetate and lead aspartate. The cryofixation by high-pressure freeze and freeze-substitution (HPF-FS) better preserves membrane quality, while the OTO adds to the final contrast compared to a single exposure to osmium.

Live dauers were immediately transferred into a bacterial slurry in a type A hat, matched to a sapphire disk to close the volume, backed by a type B hat (flat side towards sapphire disk) and mounted into the specimen holder of a Bal-tec HPM010 High Pressure Freezer. The samples were frozen under high pressure and moved to the first fixative, 5% glutaraldehyde, 0.1% tannic acid in acetone, at liquid nitrogen temperature. Multiple samples from the same run could be fixed in the same tube to conserve space in the freeze substitution device, and assure that portions of samples are well-frozen.

Frozen samples were moved into a Leica freeze substitution device at a holding temperature of -90°C and held at that temperature for 64 hours, then warmed to -60°C in 5°C steps and held for another 48 hours. During this time, samples were washed several times in dry cold 98% acetone, then shifted to the second fixative, 2% osmium tetroxide, 0.1% uranyl acetate, 2% double-distilled (DD) water in acetone. After 48 hours, temperature was then raised slowly to -30°C in 5°C steps and held at -30°C for 16 hours. Then, it was immediately followed by four washes in 98% cold acetone for 15 minutes each. Samples were removed from the freeze substitution unit and put onto ice, then transferred to 0.2% thiocarbohydrazide in acetone for one hour at room temperature. After four 15-minute washes in 98% acetone, the samples were moved to the third fixative, 2% osmium tetroxide, 0.1% uranyl acetate, 2% DD water in acetone on ice for one hour. After three 10-minute washes in 98% acetone at room temperature, the samples were stained in 1.5 ml of filtered 2% lead aspartate in acetone for 15 minutes at room temperature. The samples were transferred to microporous specimen capsule (EMS, cat # 70187-21) for further handling of multiple worms without sample losses.

The samples were washed four times in 100% acetone for 15 minutes each at room temperature. Stepwise infiltration with resin:acetone dilutions (1p:2p and 2p:1p) was performed. Individual animals were mounted on Lab-Tek chamber slides with cover glass slide (EMS, cat # 70411) as molds. Then, cover glass was removed and the samples were cured in a 60°C oven for 48 hours, which makes it possible to cut out single animals from a thin layer of resin and Aclar to remount for thin sectioning.

Electron microscopy image acquisition for dauer larvae

RMC PowerTome XL Ultramicrotome (Boeckeler Instruments, Inc.) and a 45-degree Ultra Diamond Knife (Electron Microscopy Sciences, cat # 40-US) were used for sectioning at a speed of 1 mm/s to cut 50 nm serial sections. The sections were collected onto Formvar-coated slot grids by hand [37].The sections were post-stained, first with 2% uranyl acetate for 20 minutes, and then a 1:5 dilation of Reynold's lead citrate for 5 minutes.

Transmission electron microscopy imaging was conducted on a JEOL JEM-1400Plus microscope, equipped with a Gatan Orius SC1000B bottom mount digital camera. Using Serial EM software, we collected about 70 individual images per thin section.

Stitching and alignment

Stitching and alignment for dauer EM images were done using TrakEM2 software [38]. First of all, image patches were normalized to have similar contrast and brightness. Scale-invariant feature transform (SIFT; [39]) was applied to identify local features in the overlapping area of the adjacent image patches. Based on identified features, optimal affine transformation was computed, which minimizes least squares error, then applied to stitch image patches.

To align the stitched image sections, the total image stack was divided into multiple chunks of image sections and each chunk was aligned separately to prevent large distortion. For each chunk, image features were manually selected from the first and last sections, then the affine transformation parameters that minimize least square error were computed. Transformations for intermediate sections were computed by interpolation according to the section's distance from the first and last sections. Affine transformation with manual features was applied to align the chunks. Lastly, elastic alignment in TrakEM2 was applied for the final alignment of the image stack.

Volumetric reconstruction and cell identification

Every neuron, muscle, glia processes were volumetrically segmentation. Using VAST software [40], centers of neurons were manually traced first, and then cell volumes were reconstructed. Left and right orientation were concluded with asymmetric ventral nerve cord. The neurons were identified by anatomical features such as location of soma, neurite trajectory, relative positions with neighborhood, distinctive morphological traits as described, and checked with comparison of other EM datasets [1, 12-14]. Neuron type classification were followed by previous research [12].

Chemical synapse detection and synaptic partner assignment

Two areas of the volume have been selected from the EM volume and 10 sections from each area have been chosen to be annotated for the ground truth labels. Human annotators painted presynaptic active zones, which are darkly stained pixels near the membrane, using VAST [40] and the results have been reviewed by another annotator. Ground truth labels covering an area of 9053 μm^2 have been generated. The labels have been divided into train (7340 μm^2), validation (874 μm^2), and test (839 μm^2) datasets.

The network used for the chemical synapse detection was adopted from 2D symmetric U-Net architecture [41]. The architecture was composed of five layers with a number of feature maps 16, 32, 64, 128, 256 from the top most layer to the bottom most layer, respectively. For each step in downsampling and upsampling layers, the architecture consisted of three 3 x 3 non-strided same convolutions. In the downsampling layers, max pooling was used to downsample by a factor of 2 in each layer. In the upsampling layers, a transposed convolution layer with nearest neighbor interpolation followed by 2 x 2 non-strided convolution was used to upsample by a factor of 2 in each layer. Skip connection was included in every layer which concatenates feature maps at the same level of the left hand side to the output of the transposed convolution layer. Instance normalization [42] and rectified linear unit (ReLU) was added after each 3 x 3 convolution. At the end of the symmetric network, 3 x 3 non-strided same convolution and sigmoid function was applied to produce the same-

sized output image, where each pixel value represents probability of each pixel belonging to the presynaptic active zone. The network takes an input EM image that has patch size of 576 x 576 pixels in 2 x 2 nm^2 resolution and outputs an image with size of 512 x 512 pixels in the same resolution. Note that the input image is 64 pixels larger in each dimension as 32 pixels from the edges have been cut off to avoid inaccurate predictions near the borders.

The network has been trained using an Adam optimizer [43] and using binary cross entropy as a loss function. The learning rate has been kept constant at 0.0005. Horizontal and vertical flip and multiple of 90-degree rotation were applied on training samples as data augmentation. Also, brightness and contrast augmentation have been applied.

From the predicted probability map of active zones, we thresholded the image with a pixel threshold of 90 / 255 (35%) and generated binarized prediction images of active zones. To reconstruct active zones in 3D, we applied connected components with connectivity of 26. The errors in resulting reconstructions were corrected manually.

For each active zone, we ran Monte Carlo simulation of neurotransmitter diffusion [13] to identify potential synaptic partners. We assigned synapses sizes for each synaptic partner according to the proportion of particles that reached its segment.

Generation and modification of transgene constructs

All constructs in this study were created using Gibson assembly cloning kit (E5510; New England Biolabs). DNA fragments were inserted into the GFP vector (pPD95.77) and mCherry vector (pPD117.01; modified to mCherry red fluorescence). For transcriptional fusion constructs, we inserted the promoter region of relevant genes into vectors. The indicated numbers are relative to the start codon ATG for each gene, respectively: *egas-4p::gfp* (-279, -1); *twk-3p::Chrimson::*SL2::*mCherry* (). All details of transgene constructs are available on request.

Generation of transgenic animals

To generate transgenic animals, we microinjected DNA and plasmid constructs into the gonad of young adult hermaphrodite as a canonical method [44]. We used following co-injection marker with indicated concentration for transgenesis to isolate transgenic progeny of microinjected hermaphrodite: *unc-122p::ds-red* (25 ng/ul; red fluorescent coelomocyte) and *myo-3p::mCherry* (50 ng/ul; red fluorescent muscle). Plasmid DNAs used for microinjection were extracted and purified using a plasmid purification kit. All details of transgenic animals are available on request.

Fluorescence microscopy

Images of worms were acquired using the confocal microscope (ZEISS LSM700; Carl Zeiss). For imaging, transgenic worms were paralyzed with 3 mM levamisole and mounted on 3% agar pads. To examine the morphological and synaptic changes of neurons, we visually inspected neurons by maximum intensity projection using ZEN software (Carl Zeiss).

Contact matrices and contact area

In non-dauer datasets except for adult-1 dataset, which does not have segmentation images, segments in the region from where the nerve ring begins to the entry point of the ventral nerve cord (approximately 12~13 μm length in L2 and L3) were used to compute contact matrices for fair comparison between different size image volumes. Reasonable background masks were obtained by manually annotating the dilated results of all segments. Each segment was dilated one at a time in pseudo-random order repeatedly until the background masks were fully covered. As non-dauer datasets do not have cell bodies and long amphid processes segmented, these segments were removed from the dauer segmentation images when computing contact matrix.

To measure the contact area between cell segments, contact direction (i.e. x-y, x-z, or y-z) was identified for each voxel in the contact region. For each contact voxel, the area of the square orthogonal to the contact direction was measured, and contact area was calculated as the sum of the areas for all contact voxels. For fair comparison of contact areas between datasets, contact areas have been normalized by the standard deviation of connection weights without the top 5th percentile to remove the bias due to the big outliers. Then, these contact areas and normalized contact areas have been assigned to corresponding locations in the 187 X 187 (neurons) common contact matrix structure for all datasets to create contact matrices.

Connectivity matrices and connection weights

Connection weights between a connected pair of neurons were computed as the sum of all synapse sizes of synapses between pre- and postsynaptic neurons of the pair. For fair comparison of connection weights between datasets, connection weights have been normalized by the standard deviation of connection weights without the top 5th percentile to remove the bias due to the big outliers. Then, these connection weights and normalized connection weights have been assigned to corresponding locations in the 187 X 187 (neurons) common connectivity matrix structure for all datasets to create connectivity matrices.

Wiring diagrams

Network diagrams were drawn using Cytoscape [45]. In the diagram, edges with normalized connection weights below the average of individual synapse weights (w=0.2728) were excluded. Also, connections between neurons and CEPsh cells and autapses, synapses to itself, have been excluded from the diagram. Connections are drawn as arrows, indicating the direction of connections, and the width of arrows represent the connection weights. In the figures with two wiring diagrams for comparison, the color of the edges indicate the changes in normalized weights in the dauer stage. Red and blue indicate increase and decrease in the dauer stage respectively. Orange indicates dauer-specific connection.

Stage-conserved and stage-specific connections

Connections included in the intersection of all 11 datasets (Fig. 2b) were assigned as stage-conserved connections. In each dataset, the connections that only exist in the dataset and cannot be found in any of the other 10 datasets were assigned as stage-specific connections.

Nictation assay

First, We created a micro-dirt chip by pouring a 3.5% agar solution onto a PDMS mold [35]. The solidified chip was then detached from the PDMS mold and dried for 90 min at 37°C. For individual nictation assays, individual dauer were observed for 1 min and measured nictating time. Quiescent dauers were excluded from measurements. For population nictation assays, more than 30 dauer larvae were collected by a glass capillary tube using M9 isotonic buffer and mounted onto a freshly prepared micro-dirt chip. After 10–30 min, when dauers started to move, nictation was quantified as the fraction of nictating worms among moving dauers. Nictation assays were carried out at 25°C with a humidity of 30%. Assays were repeated at least four times for quantification and statistics. [9, 35]. For optogenetic experiments, young adult worms expressing Chrimson transgenes were transferred to either normal OP50 pheromone plates or OP50-retinal pheromone plates containing 1 mM all-trans-retinal (Sigma). The transgenic dauers derived from the pheromone plate were transferred to a micro-dirt chip and their behavior was recorded for approximately 1 minute under green light (510-560 nm) on a Leica M205 FA microscope. The behavior of a dauer from the OP50-retinal pheromone plate and a dauer from the normal OP50 pheromone plate was recorded alternately, and the nictation ratio was quantified from the recorded movies.

Network properties

Total of 185 neurons, excluding CAN neurons as they have no connections, were used to compute network properties. Among 185 neurons, 71 were sensory neurons, 73 were interneurons, and 41 were motor neurons. The analysis was restricted to a network of neuronal cells, excluding muscle cells and end organs, as non-neuronal cells have inconsistencies between datasets.

Out- and in-degrees of a neuron was calculated by counting the number of postsynaptic partners and presynaptic partners, respectively. Normalized out- and in-weights of a neuron was calculated by the sum of normalized synapse weights between the neuron and all postsynaptic partners and presynaptic partners, respectively. Path length between a pair of neurons is computed by counting the minimum number of steps from the source neuron to the destination neuron.

Clustering coefficient (CC) measures the probability of the pair of neurons that are connected to a common neuron being connected to each other. CC was defined as

$$CC(u) = \frac{2T(u)}{deg(u)(deg(u)-1)}$$

where $deg(u)$ is the number of edges connected to the neuron u regardless of their directions. $T(u)$ indicates the number of triangles via node u, which occurs when the two neurons connected with neuron u are connected to each other. Nodes with less than two edges were excluded from the analysis as they have no chance of forming a triangle. Besides measuring the CC of the whole network, CC has been also measured in the sensory, interneuron, and motor subnetworks which only consist of connections within the same type of neurons.

Small-worldness of a network has been measured with two measures, small-worldness (ω) and small-world index (SWI). Small-worldness measures are acquired by comparing the mean path length and clustering coefficient of the given network to those of ER random networks and lattice networks with the same number of neurons and average number of connections. Two measures are defined as

$$\omega = \frac{L_r}{L} - \frac{C}{C_l}, \qquad SWI = \frac{L - L_l}{L_r - L_l} \cdot \frac{C - C_r}{C_l - C_r}$$

where L, C are mean path length and CC of the given network, L_r, C_r are those of ER random networks, and L_l, C_l are those of lattice networks. 100 random combinations of ER random networks and lettuce networks have been generated to compute small-worldness distribution in each stage. Lattice network was generated by an edge-swapping algorithm [46] with the number of swaps set to 100, which was chosen conservatively as the average CC of generated lattice networks saturate after approximately 60 swaps.

Edge betweenness centrality (EBC) is a measure which quantifies how often a connection is used for the communication between any given pair of neurons by counting the number of shortest paths that pass through the given connection. EBC is defined as

$$EBC(e) = \sum_{s,t \in V} \frac{\sigma(s,t|e)}{\sigma(s,t)}$$

where V is set of nodes, $\sigma(s,t)$ is number of shortest path from s to t, and $\sigma(s,t|e)$ is the ones that pass through e.

Connection proportions

The neurons in the network were first assigned to one of 3 cell types: sensory, inter-, and motor neurons. Then, each connection was classified by 3x3=9 different types according to the types of pre- and postsynaptic neurons. For each connection type, connection proportion was calculated by normalizing the number of connections within the type by the total number of connections. Proportion

of stage-specific connections was defined as the ratio of number of stage-specific connections and the number of connections within the type.

Motif analysis

The whole network has been divided into three subnetworks: sensory, interneuron, and motor subnetworks. Then, the analysis has been done separately for each subnetwork, which only consists of connections within the neurons of that type. To compute the occurrences of three-cell motifs, all combinations of three cells were extracted from the binarized connectivity matrix. For each combination, it was assigned to one of 16 motif patterns depending on its connectivity. The proportion of triangular motifs was computed by dividing the sum of numbers of motifs that form triangles (motifs 10-16) by the total number of three-cell combinations among 185 neurons. Same computation has been done for 1000 ER random networks, which have the same number of nodes and connection probability, for comparison.

Statistics

Statistical tests were done by custom Python script using SciPy library. Unpaired t-tests were used to compare distributions of connection weights (Extended Data Fig. 3e) and the results of behavior experiments (Figs. 4c-e). Pearson product-moment correlation coefficients were used for compute correlation of small-worldness across development (Fig. 5d). Data point for dauer was excluded when measuring correlation since it was difficult to decide the proper position for it. Two-sided Wilcoxon rank-sum tests were used to compare distributions of EBCs of all connections and dauer-specific connections (Fig. 6c) and the distributions of CCs of motor neurons between dauer and other stages (Fig. 6e).

Limitations

As we have reconstructed only one dauer connectome, there exists a possibility that the features described in this study could be due to individual variability. We have conducted fluorescence imaging to validate certain features (e.g. IL2 morphological changes) also exist in other dauer animals but we could not validate all features. Gap junctions, another important component in the neural circuit, are not included in this study as it is difficult to identify gap junctions in our EM image dataset due to staining and fixation methods. Still, we have attempted to identify gap junctions that are obvious and the data is available along with the analysis code. Despite the above caveats, it is still the only publicly available dauer connectome dataset so we hope this resource could help the community in stage-wise comparative study of *C. elegans.*

Data and code availability

Data and analysis codes are available upon request. Requests for resources should be directed and will be fulfilled by the corresponding author, Junho Lee (elegans@snu.ac.kr).

Acknowledgments

We thank Steven J. Cook and Oliver Hobert for reagents and advice. We also thank Scott W. Emmons and Hannes E. Bülow for discussion. *C. elegans* strains were kindly provided by the Caenorhabditis genetic center (USA), and Yuichi Iino. We thank Gwanho Ko and undergraduate students for their help with cell segmentation. This research was funded by the Samsung Science and Technology Foundation (Project Number SSTF-BA1501-52). H.Yim and D.T.C. were supported by the BK21 program. J.A.B. acknowledges support by the National Research Foundation of Korea grant (2019R1A6A1A10073437) funded by the Korean government (MEST).

Author contributions

K.N. generated EM dataset after sample preparation by H.K. under supervision of D.H. B.S. stitched and aligned the images. H.K. segmented the EM images and H.Yim proofread them. J.A.B. trained and applied nets for synapses using ground truth generated by H.Yim, D.T.C. H.Yim analyzed morphology and connectivity differences in dauer with help from D.T.C and J.A.B. D.T.C analyzed network characteristics with input from J.A.B. and H.Yim. S.A. and H.Yim performed confocal experiments. M.C. conducted optogenetics experiments. M.C. and H. Yang performed nictation experiments. H.Yim, D.T.C., J.A.B., D.H., J.S.K., and J.L. wrote the paper. J.L. and J.S.K. managed the project.

Competing interests

The authors declare no competing interests.

References

1. White, J.G., et al., *The structure of the nervous system of the nematode Caenorhabditis elegans.* Philos Trans R Soc Lond B Biol Sci, 1986. **314**(1165): p. 1-340.
2. Emmons, S.W., *The beginning of connectomics: a commentary on White et al. (1986) 'The structure of the nervous system of the nematode Caenorhabditis elegans'.* Philos Trans R Soc Lond B Biol Sci, 2015. **370**(1666).
3. Cassada, R.C. and R.L. Russell, *The dauerlarva, a post-embryonic developmental variant of the nematode Caenorhabditis elegans.* Dev Biol, 1975. **46**(2): p. 326-42.
4. Golden, J.W. and D.L. Riddle, *The Caenorhabditis elegans dauer larva: developmental effects of pheromone, food, and temperature.* Dev Biol, 1984. **102**(2): p. 368-78.
5. Golden, J.W. and D.L. Riddle, *A pheromone-induced developmental switch in Caenorhabditis elegans: Temperature-sensitive mutants reveal a wild-type temperature-dependent process.* Proc Natl Acad Sci U S A, 1984. **81**(3): p. 819-23.
6. Altun, Z.F. and D.H. Hall, *Introduction. In WormAtlas. doi:10.3908/wormatlas.1.1.* 2009.
7. Gaglia, M.M. and C. Kenyon, *Stimulation of movement in a quiescent, hibernation-like form of Caenorhabditis elegans by dopamine signaling.* J Neurosci, 2009. **29**(22): p. 7302-14.
8. Hallem, E.A., et al., *A sensory code for host seeking in parasitic nematodes.* Curr Biol, 2011. **21**(5): p. 377-83.
9. Lee, H., et al., *Nictation, a dispersal behavior of the nematode Caenorhabditis elegans, is regulated by IL2 neurons.* Nat Neurosci, 2011. **15**(1): p. 107-12.
10. Albert, P.S. and D.L. Riddle, *Developmental alterations in sensory neuroanatomy of the Caenorhabditis elegans dauer larva.* J Comp Neurol, 1983. **219**(4): p. 461-81.
11. Britz, S., et al., *Structural Analysis of the Caenorhabditis elegans Dauer Larval Anterior Sensilla by Focused Ion Beam-Scanning Electron Microscopy.* Front Neuroanat, 2021. **15**: p. 732520.
12. Cook, S.J., et al., *Whole-animal connectomes of both Caenorhabditis elegans sexes.* Nature, 2019. **571**(7763): p. 63-71.
13. Witvliet, D., et al., *Connectomes across development reveal principles of brain maturation.* Nature, 2021. **596**(7871): p. 257-261.
14. Brittin, C.A., et al., *A multi-scale brain map derived from whole-brain volumetric reconstructions.* Nature, 2021. **591**(7848): p. 105-110.
15. Cook, S.J., C.A. Kalinski, and O. Hobert, *Neuronal contact predicts connectivity in the C. elegans brain.* bioRxiv, 2022.
16. Schroeder, N.E., et al., *Dauer-specific dendrite arborization in C. elegans is regulated by KPC-1/Furin.* Curr Biol, 2013. **23**(16): p. 1527-35.
17. Bargmann, C.I. and H.R. Horvitz, *Chemosensory neurons with overlapping functions direct chemotaxis to multiple chemicals in C. elegans.* Neuron, 1991. **7**(5): p. 729-42.

18. Telesford, Q.K., et al., *The ubiquity of small-world networks.* Brain Connect, 2011. **1**(5): p. 367-75.
19. Neal, Z.P., *How small is it? Comparing indices of small worldliness.* Network Science, 2017. **5**(1): p. 30-44.
20. Varshney, L.R., et al., *Structural properties of the Caenorhabditis elegans neuronal network.* PLoS Comput Biol, 2011. **7**(2): p. e1001066.
21. Steiner, P., *Brain Fuel Utilization in the Developing Brain.* Ann Nutr Metab, 2019. **75 Suppl 1**: p. 8-18.
22. Chi, S., et al., *Astrocytic Piezo1-mediated mechanotransduction determines adult neurogenesis and cognitive functions.* Neuron, 2022. **110**(18): p. 2984-2999 e8.
23. Banerjee, N., et al., *Distinct neural circuits establish the same chemosensory behavior in C. elegans.* bioRxiv, 2021.
24. Hallem, E.A. and P.W. Sternberg, *Acute carbon dioxide avoidance in Caenorhabditis elegans.* Proc Natl Acad Sci U S A, 2008. **105**(23): p. 8038-43.
25. Peron, S., et al., *Recurrent interactions in local cortical circuits.* Nature, 2020. **579**(7798): p. 256-259.
26. Hupe, J.M., et al., *Cortical feedback improves discrimination between figure and background by V1, V2 and V3 neurons.* Nature, 1998. **394**(6695): p. 784-787.
27. Layton, O.W., E. Mingolla, and A. Yazdanbakhsh, *Neural dynamics of feedforward and feedback processing in figure-ground segregation.* Front Psychol, 2014. **5**: p. 972.
28. Mulcahy, B., et al., *Post-embryonic remodeling of the C. elegans motor circuit.* Curr Biol, 2022. **32**(21): p. 4645-4659 e3.
29. Wolkow, C., D.H. Hall, and L.A. Herndon, *WormAtlas Dauer Handbook - The Dauer Nervous System - Behavior.* WormAtlas, 2012.
30. Izquierdo, E.J. and R.D. Beer, *From head to tail: a neuromechanical model of forward locomotion in Caenorhabditis elegans.* Philos Trans R Soc Lond B Biol Sci, 2018. **373**(1758).
31. Ramachandran, S., et al., *A conserved neuropeptide system links head and body motor circuits to enable adaptive behavior.* Elife, 2021. **10**.
32. Brenner, S., *The genetics of Caenorhabditis elegans.* Genetics, 1974. **77**(1): p. 71-94.
33. Jeong, P.Y., et al., *Chemical structure and biological activity of the Caenorhabditis elegans dauer-inducing pheromone.* Nature, 2005. **433**(7025): p. 541-5.
34. Butcher, R.A., et al., *Small-molecule pheromones that control dauer development in Caenorhabditis elegans.* Nat Chem Biol, 2007. **3**(7): p. 420-2.
35. Lee, D., et al., *Nictation Assays for Caenorhabditis and Other Nematodes.* Bio-Protocol, 2015. **5**(7).
36. Seligman, A.M., H.L. Wasserkrug, and J.S. Hanker, *A new staining method (OTO) for enhancing contrast of lipid--containing membranes and droplets in osmium tetroxide--fixed tissue with osmiophilic thiocarbohydrazide(TCH).* J Cell Biol, 1966. **30**(2): p. 424-32.
37. Hall, D.H. and W.J. Rice, *Electron Tomography Methods for C. elegans.* Methods Mol Biol, 2015. **1327**: p. 141-58.
38. Cardona, A., et al., *TrakEM2 software for neural circuit reconstruction.* PLoS One, 2012. **7**(6): p. e38011.
39. Lowe, D.G., *Object Recognition from Local Scale-Invariant Features.* Proceedings of the Seventh IEEE International Conference on Computer Vision, 1999.
40. Berger, D.R., H.S. Seung, and J.W. Lichtman, *VAST (Volume Annotation and Segmentation Tool): Efficient Manual and Semi-Automatic Labeling of Large 3D Image Stacks.* Front Neural Circuits, 2018. **12**: p. 88.
41. Olaf Ronneberger, P.F., Thomas Brox, *U-Net: Convolutional Networks for Biomedical Image Segmentation.* arXiv, 2015.
42. Ulyanov, D., A. Vedaldi, and V. Lempitsky, *Deep Image Prior.* International Journal of Computer Vision, 2020. **128**(7): p. 1867-1888.
43. Diederik P. Kingma, J.B., *Adam: A Method for Stochastic Optimization.* arXiv, 2014.
44. Mello, C.C., et al., *Efficient gene transfer in C.elegans: extrachromosomal maintenance and integration of transforming sequences.* EMBO J, 1991. **10**(12): p. 3959-70.

45. Shannon, P., et al., *Cytoscape: a software environment for integrated models of biomolecular interaction networks.* Genome Res, 2003. **13**(11): p. 2498-504.
46. Sporns, O. and R. Kotter, *Motifs in brain networks.* PLoS Biol, 2004. **2**(11): p. e369.